Global dynamics and integrity of a micro-plate pressure sensor

Global dynamics and integrity of a micro-plate pressure sensor

P. Belardinelli[a,b,*], B. Sajadi[a], S. Lenci[b], F. Alijani[a]

[a]*Precision and Microsystems Engineering, TU Delft, Delft, The Netherlands*
[b]*DICEA, Polytechnic University of Marche, Ancona, Italy*

Abstract

This paper investigates the complex bifurcation scenario of electrically-actuated circular micro-plates subjected to differential pressure. Our analysis deals with the primary, secondary and ultimate saddle-node bifurcation points responsible for the device snap-through and addresses the pressure range in which the robustness of the two main stable configurations is undermined by minor coexisting attractors. By making use of basins of attraction and integrity profiles, safe dynamical regions of motion are evaluated with respect to the applied DC voltage. It is found that period-doubling bifurcations are accountable for a sensible reduction in the dynamical integrity, small variations of the DC voltage largely modify the response of the pressure sensor.

Keywords: Basins of attraction, micro-plate, dynamical integrity, bifurcations

1. Introduction

Micro-Electro-Mechanical Systems (MEMS) are being vastly developed as sensors and actuators for various engineering applications [1, 2]. Proper device fabrication is always in search of new design tools that minimize the trial and error steps involved in realization of the device. Because of the nonlinear nature of these devices, many applications require cancellation of nonlinearities since they can affect the efficiency and may lead to failure. In turn, nonlinearities are often used for achieving better performances, an example is the electrostatic instability that is exploited for trigging switches and sensors [3, 4]. Irrespective of the application at hand, mastering the overall dynamical behavior represents the vital step towards the functionality of MEMS [5, 6, 7].

Mechanisms relying on nonlinear dynamics demonstrate great potentiality for bifurcation-based sensors with high sensitivity that exploit the multi-stability of the response. Exemplary applications are detection of gas molecules [8, 9] and labelling of particles by using fully-clamped/cantilever microresonators [10, 11].

In order to unveil instability regions and their relative extensions with respect to the governing parameters, a global analysis has to be fulfilled. By studying the evolution of the response, as time goes to infinity, towards special solutions, namely, attracting sets, it is possible to label the behaviour of dynamical systems. This assumes vital importance in nonlinear systems that may be characterized by multistable behaviour, i.e. possess a variety of attractors. [12].

Basins of attraction are maps that show all the possible outcomes of a dynamical system, by definition, subsets of the phase space (sets of initial conditions) bringing the system to converge to a specific attractor. These maps allow to asses the real stability of the system, theoretically fully

*Corresponding author: P. Belardinelli, Department of Precision and Microsystems Engineering, Research group of Dynamics of Micro and Nanosystems, 3ME, Mekelweg 2, (2628 CD) Delft, The Netherlands. Email: p.belardinelli@tudelft.nl

bounded in the classical, or Lyapunov, sense [13]. Indeed, it is evident that only if the system is able to accommodate finite perturbations it can be considered safe from a practical point of view. Thus, the determination of attractors, unstable orbits (e.g. saddles, homo-heteroclinic), and their bifurcations, within a local point of view does not suffice. Theoretically stable solutions may be not visible in practice [14], when their basins of attractions are not large enough, thus being not robust and practically unstable. All of this, call for an in-depth global analysis of the dynamic system at hand. Surprisingly, despite the usefulness and the great potential of the approach, its implementation in MEMS devices is still essentially rather scant.

Determination of domains of attraction, beside few and paradigmatic cases, is based on numerical techniques computationally expensive with large time consumption, especially for high-dimensional systems in which a system reduction greatly deprecate the reliability of results [15]. Remarkable improvement in computational algorithm have thus been proposed [16, 17]. These approaches permit to analyze in reasonable computational time, a large set of initial conditions with sufficient resolution to determine properly basins of attraction of the system.

In this paper we obtain basins of attraction for a circular parallel-plate pressure sensor that exhibits intricate dynamics upon electrical actuation. An electric potential is applied between the lower, fixed, and the upper flexible electrode. The deformation of the flexible plate are detected by capacitive changes of the system [18, 19] and can be exploited for sensing operations. Conversely, in the actuation mode, the output of the device is induced by the electric potential.

The electrostatic load comprises an applied bias (DC voltage) and an alternating (AC voltage) component that introduces nonlinearity in the system, i.e. the electrical force is a nonlinear function of the distance between the two electrodes. An additional source of nonlinearity is geometrical. Within the elastic potential, a nonlinear term accounts for finite defections of the electrode. The combination of these two nonlinearities eventually results in a softening or hardening nonlinear dynamic behaviour [20].

Particular combinations of DC and AC voltages lead the motion of the plate to become unstable and yield pull-in (or snap-through) phenomenon [21, 22]. The static pull-in phenomenon has been the subject of many studies, based on analytical [23, 19] or numerical [24, 25, 26] approaches. These methods have already been comprehensively reviewed in Ref. [18]. Although depending on geometry and gap-size, the static pull-in often occurs at 51-71% of the initial gap [27, 28].

The global stability in presence of AC component is more involved. Dynamic pull-in phenomenon as well has been tackled with analytical and numerical methods [22]. Dynamical instability can be observed at much lower voltages with respect to the static pull-in [21]. Furthermore, the pull-in threshold (the critical deflection at which the device collapses) is largely influenced by additional mechanical loads.

The inclusion of a differential pressure results common practice in MEMS applications [29], such as differential pressure in the case of MEMS pressure sensors. To date, though, the overall dynamics of such systems close to bifurcation points has not received much attention, and the nonlinear dynamical integrity of MEMS pressure sensors has been elusive. However, actual researches pay inadequate attention to the overall dynamical behavior of micro-plate close to instability and relative triggering factors.

This paper is meant to investigate the global nonlinear dynamics of an electrically-actuated circular micro-plate subjected to differential pressure. The governing equations of motion are obtained by using a Lagrangian approach accounting for the nonlinear stretching, and electrostatic load. A reduced order model developed in the previous studies is used to study the nonlinear dynamics of the device [23, 30, 31]. Periodic solutions and instability points are detected by making use of a pseudo arc-length continuation and collocation technique [32]. A parametric study is undertaken,

varying DC driving voltage and the differential pressure close to the bifurcation points. Basins of attraction are analysed in order to evaluate the practical stability of the system. Integrity measures are accordingly evaluated [33].

2. Problem formulation

In this section, we propose a reduced order model for dynamics of a clamped micro-plate, as the flexible electrode in a capacitive pressure sensor. A schematic illustration of the device is shown in Figure 1. The micro-plate is circular, with a radius R and thickness h, and it is assumed to be isotropic and homogeneous. Moreover, the initial gap separating the two electrodes is d. When such a device is in operation, the flexible electrode is subjected to a differential pressure (P), positive outward, and an electric potential (V) inducing an electrostatic load in the opposing direction. As a result, the micro-plate deflects from its initial flat configuration. Clearly, if the electric field has an AC component, a forced dynamic motion will be induced in the system.

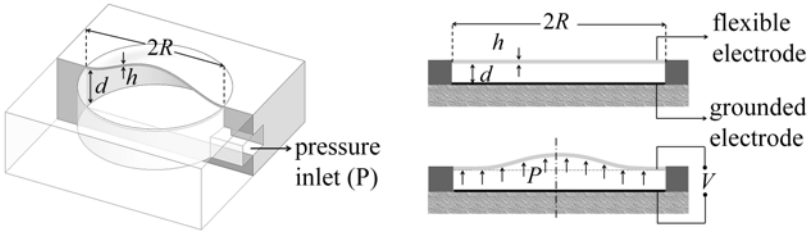

Figure 1: (a) The capacitor with upper flexible, circular electrode. (b) Plate in its undeformed configuration. (c) Deformed configuration under electrostatic load and differential pressure.

In order to obtain the equations of motion, a Lagrangian approach is utilized. Due to the radial symmetry in both geometry and the applied loads, we assume the problem to be axisymmetric [34]. In fact, if the plate is excited around its fundamental frequency without occurrence of internal resonances, even if other modes (including the anti-symmetric modes) are accidentally excited, they will decay with time due to the presence of damping. Therefore, the only contributing displacement components, are in the radial (u) and transverse (w) directions, and are functions of the radial coordinate (r), only. Consequently, the displacement field can be approximated by:

$$w = q(t)d\Phi_0(\rho), \tag{1}$$

$$u = \sum_{i=1}^{N} \xi_i(t)R\Phi_i(\rho), \tag{2}$$

where, $\rho = r/R$ is the normalized radial coordinate. The functions $q(t)$ and $\xi_i(t)$ are dimensionless, time-dependent generalized coordinates. The function $\Phi_0(\rho)$ and $\Phi_i(\rho)$ are the basis functions satisfying the clamped boundary conditions, and are defined as:

$$\Phi_0(\rho) = (1-\rho^2)^2, \tag{3}$$

and

$$\Phi_i(\rho) = \rho^i(1-\rho), \qquad (i = 1,...,N). \tag{4}$$

Note that $\Phi_0(\rho)$ is a 4^{th} order polynomial representation of the first linear mode shape of the plate [20]. Next, the total potential of the system can be obtained as a function of the displacement

components and their derivatives. The total potential energy consists of three terms: (i) the potentials related to the elastic deformation in the micro-plate (U_s), (ii) the electrostatic potential (U_e), (iii) and the potential associated with the differential pressure (W).

Assuming von Kármán plate theory, the elastic potential (U_s) can be approximated by [35]:

$$\begin{aligned} U_s = & \frac{\pi D}{R^2}\int_0^1 \left(\left(\frac{\partial^2 w}{\partial \rho^2}\right)^2 + \left(\frac{1}{\rho}\frac{\partial w}{\partial \rho}\right)^2 + \left(\frac{2\nu}{\rho}\frac{\partial w}{\partial \rho}\frac{\partial^2 w}{\partial \rho^2}\right) \right) \rho d\rho + \\ & \frac{\pi E h}{(1-\nu^2)}\int_0^1 \left(\left(\frac{u}{\rho}\right)^2 + \left(\frac{\partial u}{\partial \rho} + \frac{1}{2R}\left(\frac{\partial w}{\partial \rho}\right)^2\right)^2 + \frac{2\nu u}{\rho}\left(\frac{\partial u}{\partial \rho} + \frac{1}{2R}\left(\frac{\partial w}{\partial \rho}\right)^2\right) \right) \rho d\rho, \end{aligned} \tag{5}$$

where, E, ν and μ are the Young's modulus, Poisson's ratio and density, respectively. Moreover, $D = \frac{Eh^3}{12(1-\nu^2)}$ is the bending stiffness of the flexible plate. Assuming that the loads associated with the electrostatic field and pressure maintain perpendicular to the un-deformed surface [36], the electrostatic potential reads as [18]:

$$U_e = -\pi \varepsilon V^2 R^2 \int_0^1 \frac{\rho d\rho}{d+w}, \tag{6}$$

with ε the electric permittivity of the dielectric between the plate and the ground, while, the electric potential $V(t)$ consists of a DC bias voltage V_{DC}, and an alternating AC voltage V_{AC} with an excitation frequency of Ω, i.e. $V = V_{DC} + V_{AC}\sin(\Omega t)$. Finally, the potential associated with the pressure is given by:

$$W = 2\pi P R^2 \int_0^1 w \rho d\rho. \tag{7}$$

The kinetic energy, neglecting the contribution of the in-plane inertia, can be expressed as:

$$T = \pi \mu R^2 h \int_0^1 \dot{w}^2 \rho d\rho. \tag{8}$$

Consequently, the Lagrangian of the system ($L = T - (U_e + U_b + U_s - W)$) can be obtained as a function of the displacement components and their derivatives. Using the Lagrange equations yields to a set of $N+1$ equations of motion, consisting of N algebraic equations in terms of ξ_i ($i = 1, ..., N$) and one nonlinear differential equation in terms of q. One can solve the N algebraic equations analytically and obtain a single transverse equation of motion as [37]:

$$\ddot{q}(t) + 2\zeta\omega_0\dot{q}(t) + \omega_0^2 q(t) = -\alpha_1 D q(t)^3 + \alpha_2 V(t)^2 \left(\frac{1-(q+1)F(q)}{2q(1+q)}\right) - \alpha_3 P, \tag{9}$$

where, the parameter $\omega_0 = \frac{10.32}{R^2}\sqrt{\frac{D}{\mu h}}$ is the natural frequency of the circular clamped plate. Moreover, an energy dissipation term with a modal damping ζ has been implemented in this equation. In addition, α_1 is the coefficient of geometric nonlinearity and its accuracy is defined by the number of in-plane degrees of freedom. The parameter α_2 represents the coefficient of the nonlinear electrostatic force, while α_3 is the projection of the pressure onto the assumed mode shape in transverse direction:

$$\begin{aligned} \alpha_2 &= 2.50\frac{\varepsilon}{\mu h d^3}, \\ \alpha_3 &= 1.67\frac{1}{\mu h d}. \end{aligned} \tag{10}$$

The term $F(q)$ in Equation (9) derives from the analytical integration of the electrostatic potential in Equation (6) as:

$$\begin{aligned} F(q(t)) &= \frac{\operatorname{atanh}\sqrt{-q(t)}}{\sqrt{-q(t)}} && \text{if } q(t) < 0, \\ F(q(t)) &= 1 && \text{if } q(t) = 0, \\ F(q(t)) &= \frac{\operatorname{atan}\sqrt{q(t)}}{\sqrt{q(t)}} && \text{if } q(t) > 0. \end{aligned} \tag{11}$$

Equation (9) describes the nonlinear axi-symmetric motion of a circular clamped micro-plate, loaded with a uniform differential pressure and electrically actuated by its fundamental mode and can be numerically solved for the bifurcation analysis.

3. Numerical analysis

The procedure outlined in previous sections is used in this section to numerically study a silicon micro-plate with the following properties: $E = 169\,\text{GPa}$, $\nu = 0.17$, $\mu = 2328\,\text{kgm}^{-3}$, $h = 0.6\,\mu\text{m}$, $R = 100\,\mu\text{m}$ and $d = 2\,\mu\text{m}$. The electric permittivity of air $\varepsilon = 8.854 \times 10^{-12}\,\text{F/m}$ has been considered for the gap between the electrodes. Hence, the coefficients in Equation (9) are obtained as: $\alpha_1 = 4.139 \times 10^{21}$, $\alpha_2 = 1.981 \times 10^{9}$, $\alpha_3 = 5.978 \times 10^{8}$, $\omega_0 = 1.545 \times 10^{6}$ rad/sec, $D = 3.132 \times 10^{-9}$ Nm. Moreover, a damping ratio of $\zeta = 0.004$ is used.

3.1. Bifurcations scenario

In order to perform the bifurcation analysis, it is assumed that the plate is under the action of both AC and DC voltages. Moreover, the solution branches are obtained for a range of DC voltages for a fixed AC voltage and $\Omega/\omega_0 = 1$.

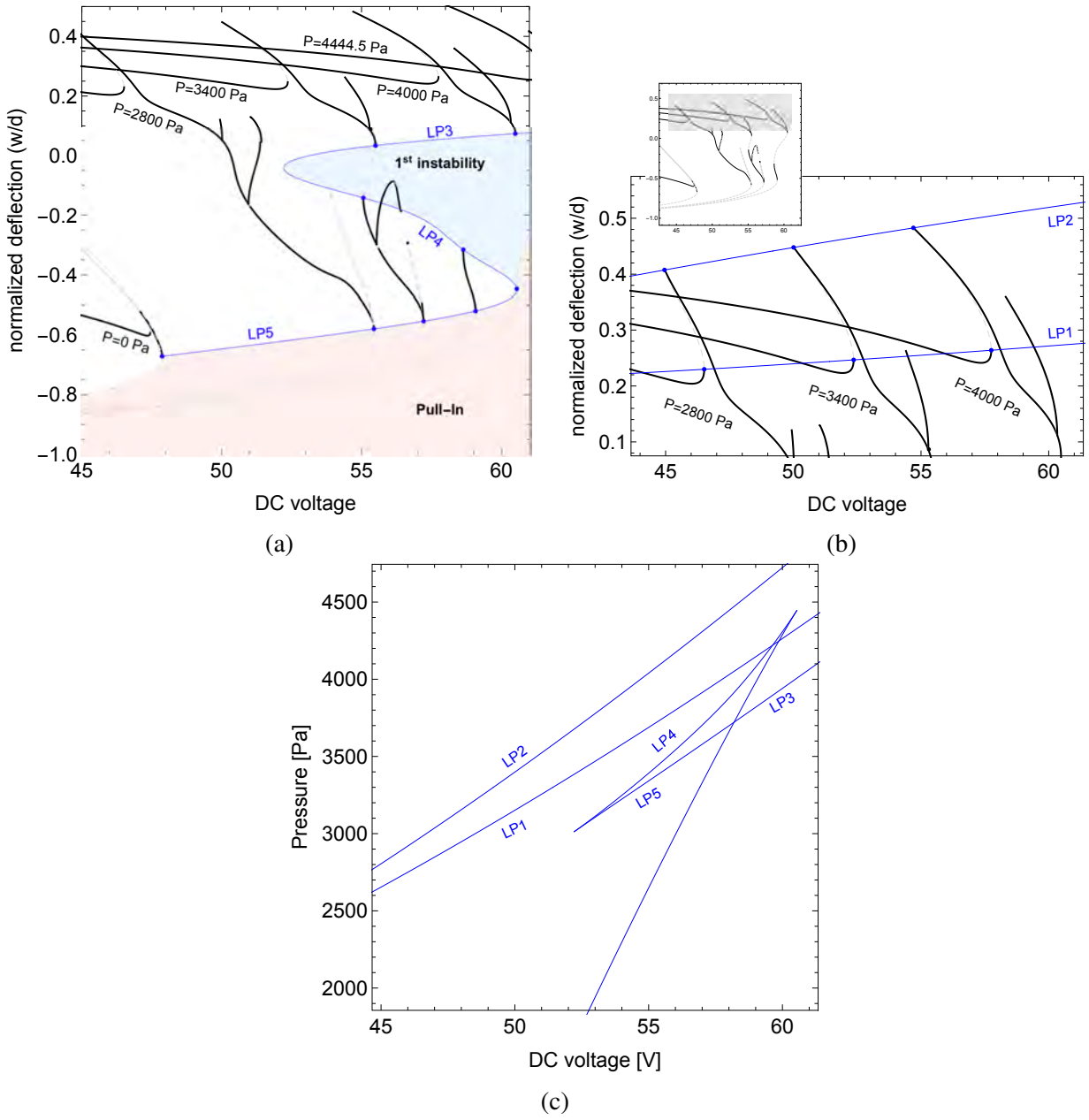

Figure 2: a) The maximum normalized deflection of the micro-plate as function of the applied DC voltage. $P = \{0, 2800, 3400, 4000, 4444.5\}\, Pa$, $V_{DC} \in [45, 61]\, V$. b) Limit points of the primary resonance (LP1, LP2) of the micro-plate, $V_{DC} \in [44, 61]\, V$. c) Bifurcation map of the limit points of the primary resonance (LP1, LP2) and of the primary (LP3), secondary (LP4) and ultimate (LP5) instability limit point ($P \in [2000, 4600]\, Pa$). Parameters: $V_{DC} \in [45, 61]\, V$, $V_{AC} = 0.1V$, $\Omega/\omega_0 = 1$.

Figure $2(a)$ shows the normalized deflection of the center of the plate (w/d) as a function of the applied DC voltage. Different values of the differential pressure P are also considered, namely $P = \{0, 2800, 3400, 4000, 4444.5\}\, Pa$. Low pressurized systems (e.g. $P = \{0, 2800\}\, Pa$) are distinguished by the presence of only one critical saddle-node bifurcation point, i.e. LP5. At this point, a slight increase of the actuation voltage brings the system to instability. The micro-plate collapses towards the reference electrode through the so-called *pull-in*. This configuration is highlighted in Figure $2(a)$ with a shaded pink area. For larger pressure values (e.g. $P = \{3400, 4000, 4444.5\}\, Pa$), the system presents an additional unstable configuration. The values at which this instability oc-

curs are depicted in Figure $2(a)$ by means of a shaded blue area. Depending on the shape of the normalized deflection curve, after the primary saddle-node LP3, the system can: i) collapse to the fixed electrode snapping through the pull-in (e.g. curve at $P = 4000Pa$); ii) recover the stability in the lower stable branch between the saddle-nodes LP4 and LP5 (e.g. curve at $P = 3400Pa$).

The quantitative thresholds for the first (LP3), secondary (LP4) and ultimate (LP5) instability points are reported in Figure $2(c)$ with the use of a pressure/voltage bifurcation chart. The two cusps at $\{V_{DC}, P\} = \{60.54V, 4444.5Pa\}$ and $\{52.21V, 3011.7Pa\}$ represent the lower and upper boundaries for the existence of a double snap-through of the micro-plate, otherwise characterized by a unique instability. In addition, Figure $2(c)$ maps the lower (LP1) and upper (LP2) saddle-node points of the primary resonance. Indeed, the alternating voltage V_{AC} introduces a nonlinear resonance in the upper stable branch of the response as shown in Figure $2(b)$. The response is characterized by a softening behaviour. The variation of the saddle-node points LP1 and LP2 with respect to V_{DC} highlights an increment in the amplitude of the resonance peak with the applied pressure.

Between the primary resonance and the first snap-through point LP3, the system manifests a subcritical period-doubling bifurcation as shown in Figure $3(a)$. The stable motion is recovered only at the limit point LP6 where a new stable period-2 branch is generated. The supercritical point PD2 returns the motion to the main branch.

The micro-plate shows an additional couple of flip bifurcations, named as PD3/4 and reported in Figure $3(b)$. They can lie: i) on the sole stable main branch in the absence of the primary and secondary instability points LP3 and LP4 (see $P = 2800Pa$ in Figure $3(b)$), ii) on the secondary stable branch before the pull-in otherwise (see $P = 3400Pa$ in Figure $3(b)$).

Similar to the first flip bifurcation, PD1, where a unique stable branch exists between PD2 and LP6, the period doubling bifurcation PD3 evolves through an unstable branch to the limit point LP7. Here, the new stable branch with period-2 motion terminates at the supercritical bifurcation PD4 as can be observed in the curve with $P = 3400Pa$ in Figure $3(b)$. This scenario holds only for specific differential pressure. Based on the complexity of the behaviour, it can be argued that the system response becomes more intricate with large values of the differential pressure.

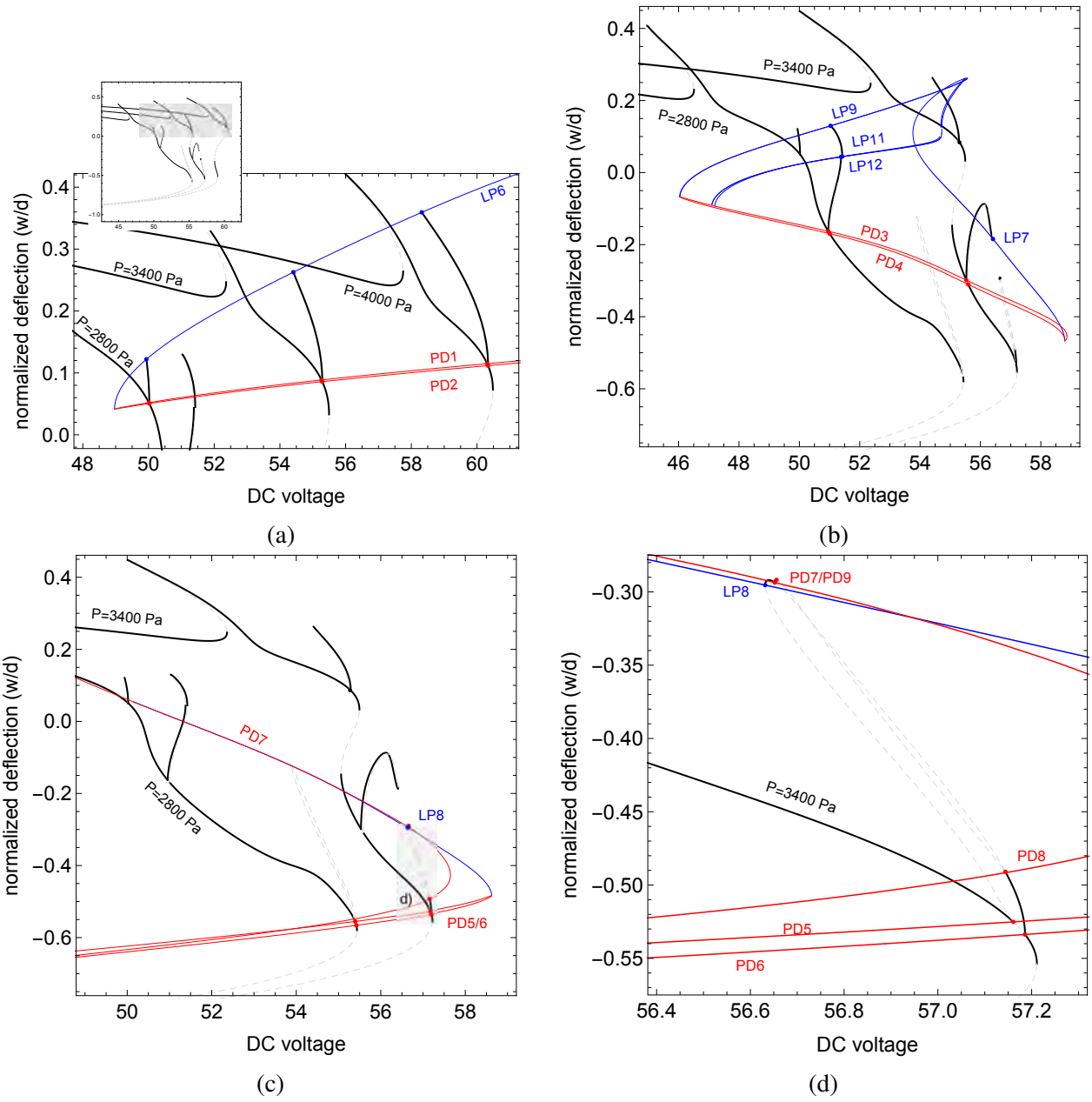

Figure 3: The maximum normalized deflection of the micro-plate as function of applied DC voltage. Saddle-node and period-doubling bifurcation points are tracked by means of blue and red lines, respectively. a) First period-doubling bifurcation (PD1, PD2) on the upper branch of the normalized deflection of the micro-plate, $V_{DC} \in [48,62]V$. $P = \{2800,3400,4000\}Pa$, $V_{AC} = 0.1V$, $\Omega/\omega_0 = 1$. The inner plots show the analysed area with respect to Figure2(a) b) Second period-doubling bifurcation (PD3, PD4) of the normalized deflection of the micro-plate. $P = \{2800,3400\}Pa$, $V_{DC} \in [44,60]V$. c) The maximum normalized deflection of the micro-plate as function of applied DC voltage. $P = \{2800,3400\}Pa$, $V_{DC} \in [53.5,55.5]V$. Third period-doubling bifurcation (PD5, PD6) of the normalized deflection of the micro-plate. d) Bifurcation diagram zoom-in of Fig. $3(c)$, $V_{AC} = 0.1V$, $\Omega/\omega_0 = 1$.

Of particular importance, is the flip bifurcation occurring close to the limit point LP5 as illustrated in Figure $3(c)$. Subcritical/supercritical symmetry-breaking bifurcations PD5/PD6 interrupt the stability of the main branch. The stability is recovered only in a limited extended branch (LP8 to PD7) in the upper part of the loop generated by PD5/PD6 (see Figure $3(d)$). An additional period doubling is generated in PD9 which unstable branch connects to PD8. The latter is responsible for the interruption of the stable period-2 motion in PD6.

Figures 2 and 3 provide a good understanding of the number and type of bifurcations taking place in the system. In order to provide the numerical thresholds at which they occur, the bifurcation loci are summarized in Figure 4 by means of DC-voltage versus pressure charts. A multitudinous intersection of locus can be observed. Instability and change in the device motion can be also reached in several regions.

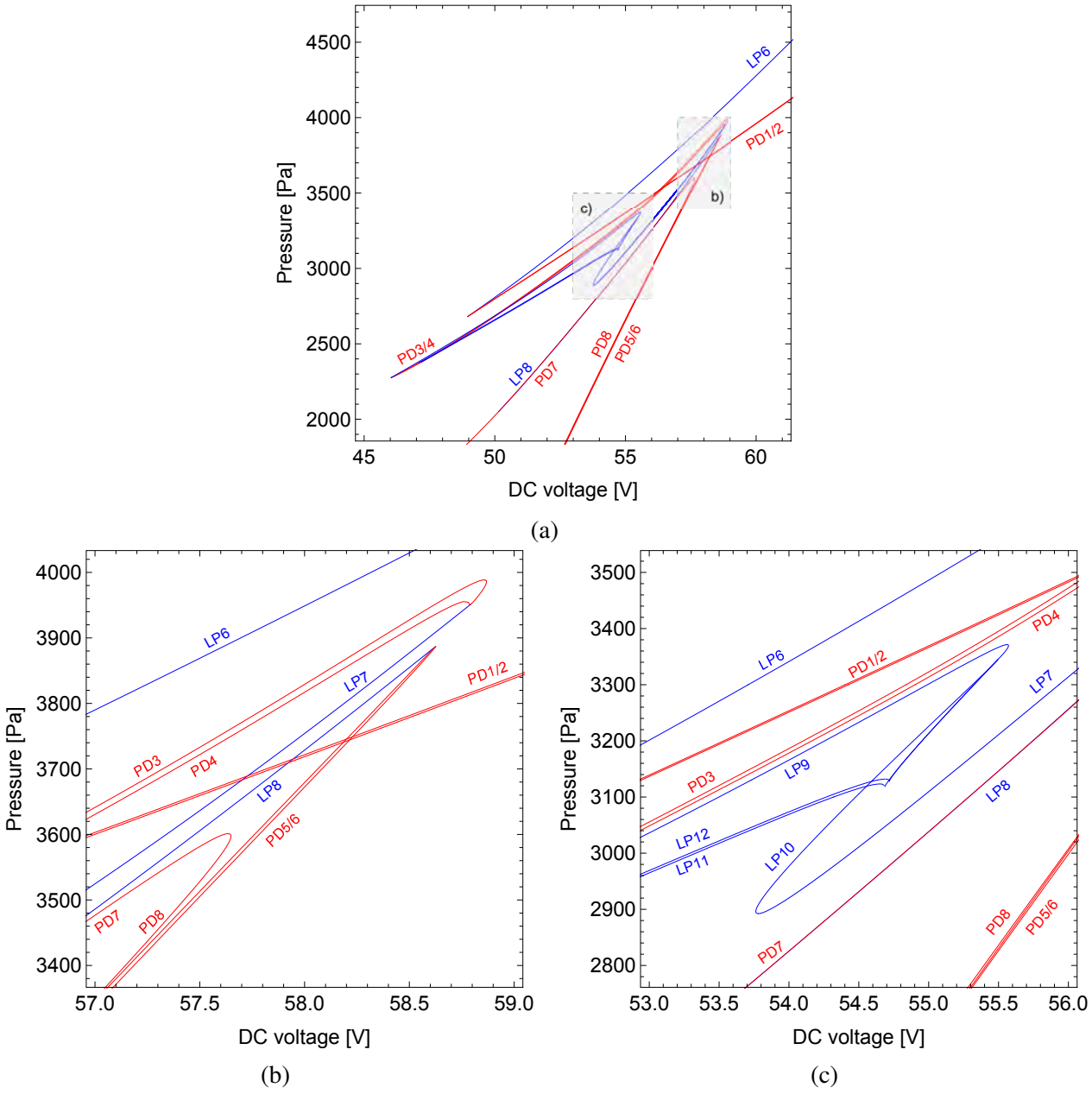

Figure 4: a) Maps of bifurcation points for the normalized maximum deflection of the micro-plate. Range of parameters: $P \in [2000, 4600]\,Pa$, $V_{DC} \in [45, 61]\,V$. $V_{AC} = 0.1V$, $\Omega/\omega_0 = 1$. b) Bifurcation maps zoom-in $P \in [3400, 4000]\,Pa$, $V_{DC} \in [57, 59]\,V$. c) Bifurcation maps zoom-in $P \in [2800, 3500]\,Pa$, $V_{DC} \in [53, 56]\,V$, $V_{AC} = 0.1V$.

Period-doubling bifurcations PD3/4 and PD1/2 appear only for a combination of {Voltage, Pressure} greater than $\{46.02V, 2277.1Pa\}$ and $\{48.95V, 2679.9Pa\}$, at these configurations they collapse to LP9 and LP6, respectively. Figures $4(c)$ zoom on a particularly dense region of bifurcations. Figures $4(b)$ highlights configurations above $3400Pa$, the vanish of the important flips

PD5/6 happens at $\{58.62V, 3888.2Pa\}$ whereas PD1/2 persist in a larger range of voltages.

3.2. Transition between the primary and the secondary stable branch

In view of the aforementioned bifurcations scenario, the dynamical response cannot be properly assessed only by observing the local behaviour. In particular, the presence of the period-doubling bifurcations close to the primary instability modifies the global dynamic of the system. For this reason, this section presents basins of attraction for the electrically-actuated micro-plate around the saddle-node points LP3 and LP4 (limit points that separate the two main stable branches). In what follows, the attractors before LP3 and after LP4 are referred as primary and secondary. Figure 5 reports the normalized deflection of the center of the plate for the configuration $P = 3300Pa$, $V_{ac} = 0.1V$, in which the two distinct branches of period-1 motion can be observed.

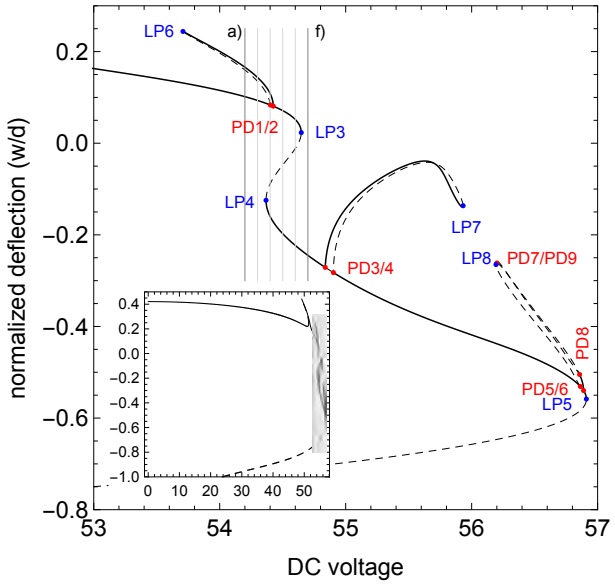

Figure 5: The maximum normalized deflection of the micro-plate as function of applied DC voltage. $P = 3300Pa$, $V_{ac} = 0.1V$, $\Omega/\omega_0 = 1$.

In this layout, domains of attraction are built in the transition between the first and the second branches by fixing the value of the DC voltage as illustrated in Figure 5 with vertical lines.

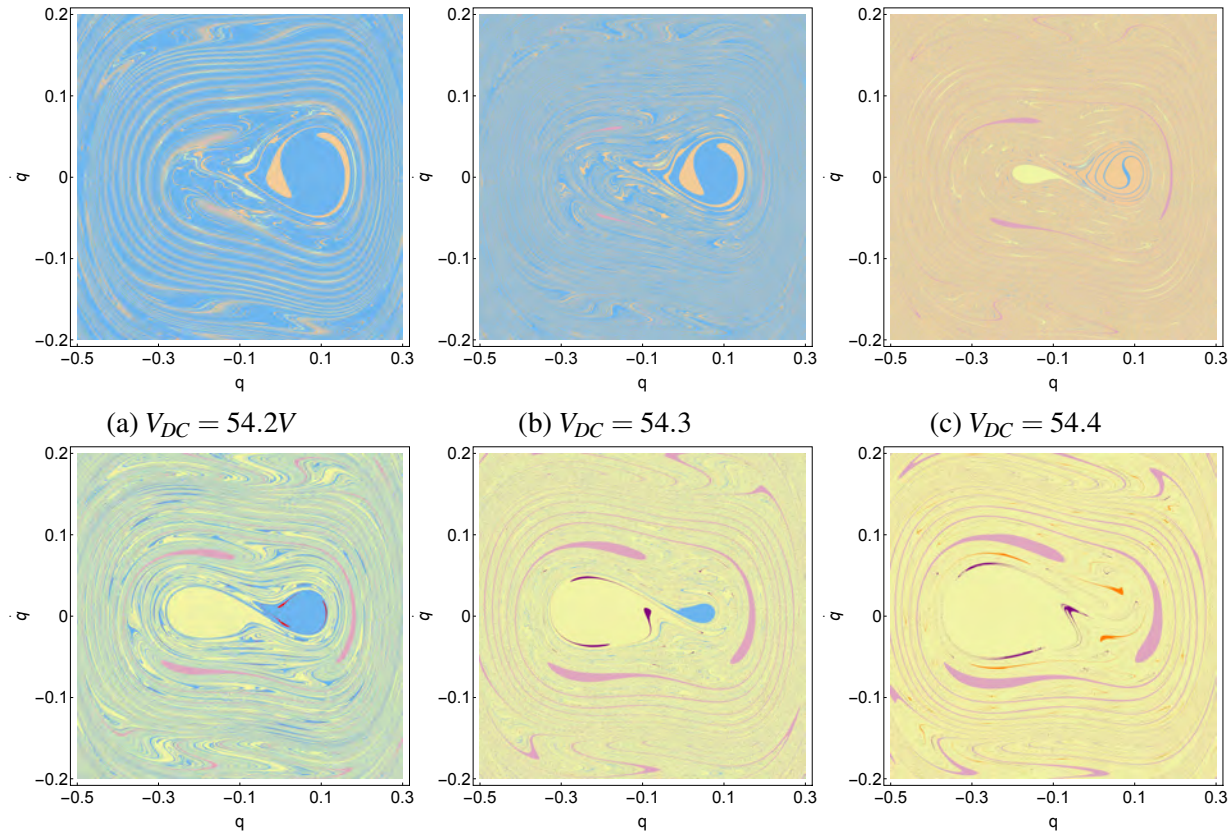

(a) $V_{DC} = 54.2V$ (b) $V_{DC} = 54.3$ (c) $V_{DC} = 54.4$

(d) $V_{DC} = 54.5$ (e) $V_{DC} = 54.6$ (f) $V_{DC} = 54.7$

Figure 6: Basins of attraction for the configurations a)-f) highlighted in Figure 5. $P = 3300Pa$, $V_{ac} = 0.1$, $\Omega/\omega_0 = 1$.

The phase-space for $V_{DC} = 54.2$ (Figure 6(a)) is primarily governed by the the period-1 attractor of the primary branch and the period-2 attractor from the PD2 bifurcation (blue and ocher basins). Increasing the voltage, the basin of the period-2 attractor becomes predominant at $V_{DC} = 54.4V$. Figure 6(c) highlights the born of the second period-1 stable region (yellow basin). The basin extends as shown in Figure 6$(c-d-e)$ as the area of the primary basin recedes. The system shows the coexistence of minor attractors that do not have particular interest under the practical point of view since they lie outside the compact part of the main basins and present a relative small amplitude. Examples are the period-3 attractor in Figure 6(a) whose basins are green-coloured, or the period-4 motion (orange basin) present at $V_{DC} = 54.7V$ and illustrated in Figure 6(f). On the contrary, other attractors are responsible for the homogeneity disruption of basins, i.e. a period-3 attractor (basin of attraction in red in Figure 6(d)) lies inside the basin of the primary snap-in. A further period-3 attractor, visible in Figure 6(e) and spreading in Figure 6(f) for $V_{DC} = 54.7V$ affects the secondary basin. The windows of existence of additional attractors demand a reduced step size in the variation of the inspected parameter. Moreover, the topological extension of rare attractors requires a dense grid in order not to overlook the actual shape of the basins [38]. Figure 7 presents the domain for a rare period-9 solution at $V_{DC} = 54.35V$. Appearance and disappearance of the rare attractor are within a small windows of the DC voltage parameter, $54.25 < V_{dc} < 54.4$.

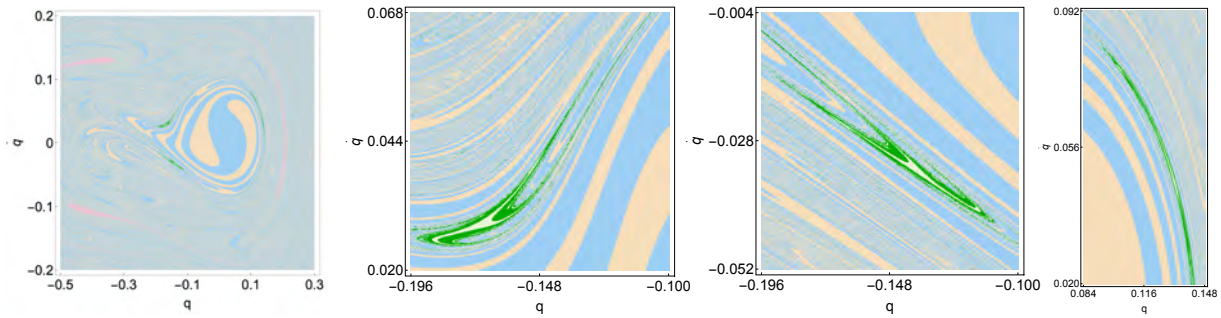

(a) (b) (c) (d)

Figure 7: Period-9 rare attractor. a) The full basin of attraction for the configuration $P = 3300Pa$, $V_{dc} = 54.35$, $V_{ac} = 0.1$. b),c),d) zoom of the basin around the period-3 attractor (light green). A grid of 5000×5000 cells for the couple $\{q, \dot{q}\}$ has been considered.

The presence of all the explained bifurcations and additional attractors imposes an investigation on the dynamical integrity of the system. This would then require the computation of a multitude of basins of attraction for different set of parameters. The confidence in the analysis of the compactness of the basins is guaranteed by the high resolution and the small steps used for the parametric variation.

3.3. Dynamical integrity

A dynamical integrity analysis is reported in this section in order to investigate the robustness of the primary and secondary attractors before the pull-in in view of all bifurcations occurring in the system. All the basins computed in this section has been built with square grid of 2000^2 cells, fine enough to evaluate the system topology.

The Local Integrity Measures (LIM) of the attractors of the system is shown in Figure 8. Although the LIM is the largest hyper-sphere (circle in 2D basins) entirely centered at the attractor of reference, for multiperiodic attractors the minimum of the measure is reported as well by using dashed lines for the sake of completeness. Figure $8(a)$ displays the variation of the LIM as a function of the V_{DC} voltage for the attractors coexisting in the system. Moreover the spatial distribution of LIMs is shown in Figure $8(b)$. Three-dimensional sweeps do not only allow for a magnitude evaluation of the measure, but also for the actual space localization with respect to the governing parameters [39]. With blue and yellow lines we refer to the primary and secondary main attractors, respectively. The system monostability on the primary basin persists up to $V_{DC} = 53.71V$ where the period doubling greatly decreases the extensions of the safe basin measured by the LIM. The basin progressively shrinks due to the positions of the PD2 attractor converging toward the period-1 attractor as shown by the integrity manifolds in Figure $8(b)$. The magnitude of the measure for the basin of the period-doubled attractor remains almost constant. In coincidence with a sudden increase of the extension of the LIM for the period-2 attractor (ocher line), the primary basin completely vanishes in $54.39V < V_{DC} < 54.43V$. The recovered LIM then starts to decrease with the born of the secondary basin (yellow line). Similarly as the primary basin, the secondary LIM disappears due to PD3. It can be noted that the LIM of the PD1 and PD3 presents a qualitative similar behaviour. With reference to Figure 5, for an increasing DC voltage, the PD1 branch encounters the saddle LP6, contrarily PD3 enters in the system with the base of branch in which the basin has maximum extension. Although, persistent over a large range of voltages ($54.15V < V_{DC} < 55.05V$), the period-3 solution depicted by purple color in Figure $6(d-f)$, does not affect the integrity of the main domains of system lying always outside without intertwining tongues. The sudden de-

crease of the LIM (purple line in Figure 8(a)) around $V_{DC} = 55V$ is determined by the born of an additional attractor inside its compact part, resulting in its disappearance.

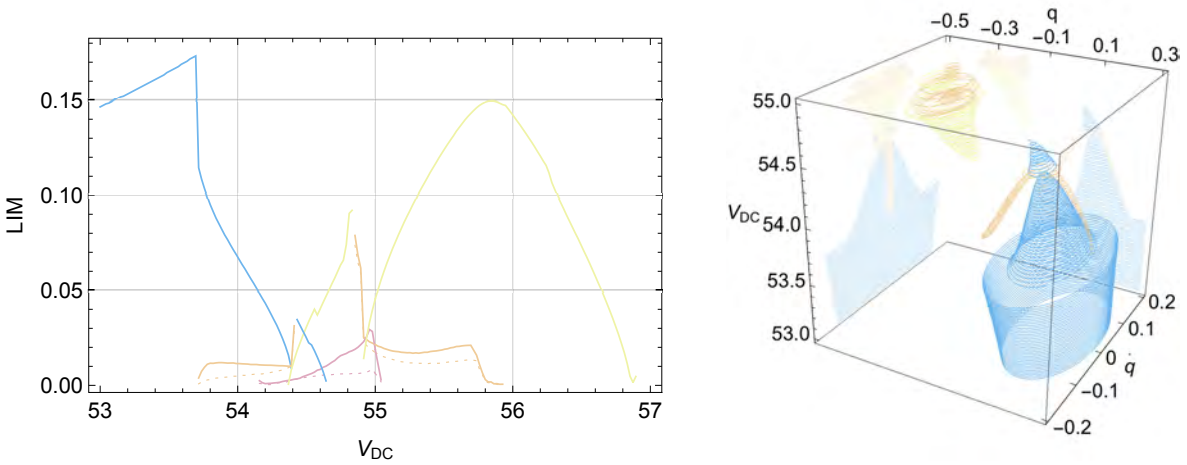

(a) (b)

Figure 8: Local integrity measure. Fixed parameters $P = 3300Pa$, $V_{ac} = 0.1$, $\Omega/\omega_0 = 1$. a) Integrity profile for the local integrity measure for $V_{DC} \in [53,57]$. ——: primary basin, ——: secondary basin, ——: basin of period-doubled attractor, ——: basin of period-3 attractor. b) Evolution of the local integrity measures in the 3D phase-parameter space for the primary and secondary basin and period-double attractors. $V_{DC} \in [53,55]$

The Integrity Factor (IF) considers the compact part of the basin, being the largest hyper-sphere within the basin (circle in 2D cases). It is a less conservative measure with respect to the LIM since it is not focused on the attractor. This is confirmed by a comparison of the magnitude of the IF in Figure 9 and the LIM in Figure 8. The integrity factor globally reflects the LIM behaviour on both integrity profile (Figure 9(a)) and spatial dislocation (Figure 9(b)). Except for an intermediate shift towards negative value of velocity ($V_{DC} = 53.9V$), the primary basis confirms the compact safe manifold with positive velocity of the phase-space. For large voltages, the IF of the secondary basin presents a concave parabolic shape with the maximum extension at $V_{DC} = 55.81V$.

The integrity measures presented in Figures 8 and 9 highlight the non-robustness of the system in the range $54.2V < V_{DC} < 55.05V$. However, these delicate thresholds also represent instability configurations to be exploited for sensing application, thus their precise evaluation is of great importance.

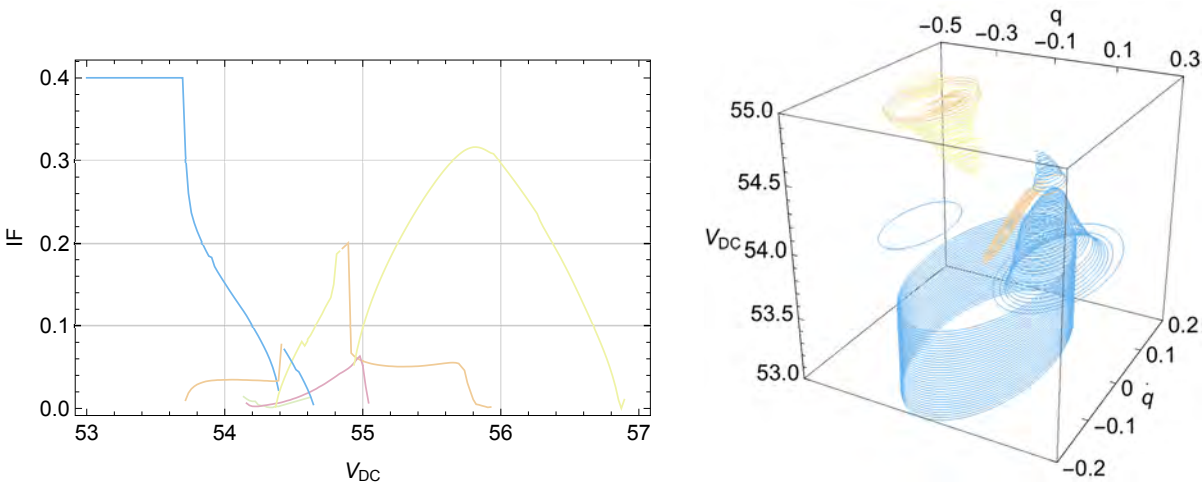

(a) (b)

Figure 9: Integrity factor measure. Fixed parameters $P = 3300Pa$, $V_{ac} = 0.1$, $\Omega/\omega_0 = 1$. a) Integrity profile for the integrity factor measure for $V_{DC} \in [53,57]$. ——: primary basin, ——: secondary basin, ——: basin of period-doubled attractor, ——: basin of period-3 attractor. b) Evolution of the integrity factor measure in the 3D phase-parameter space for the primary and secondary basin and period-double attractors. $V_{DC} \in [53,55]$.

As discussed in Section 3.1, in the secondary branch additional flip bifurcations (PD3 and PD4) are observed. The basins of attraction, coexisting with the period-doubled attractor, are shown in Figures 10. Integrity measures are calculated for all the attractors and reported in black/red circles for the LIM/IF. The conics reshape as an ellipse since the different step size in the two dimension of the phase-space. Figures $10(a,b)$ report the formation of other minor basins at the boundaries of the compact period-doubled basin (blue-coloured basin in Figures $10(a)$). This additional period-2 attractor is confined between $55V$ and $55.3158V$, as illustrated in Figures $10(c)$.

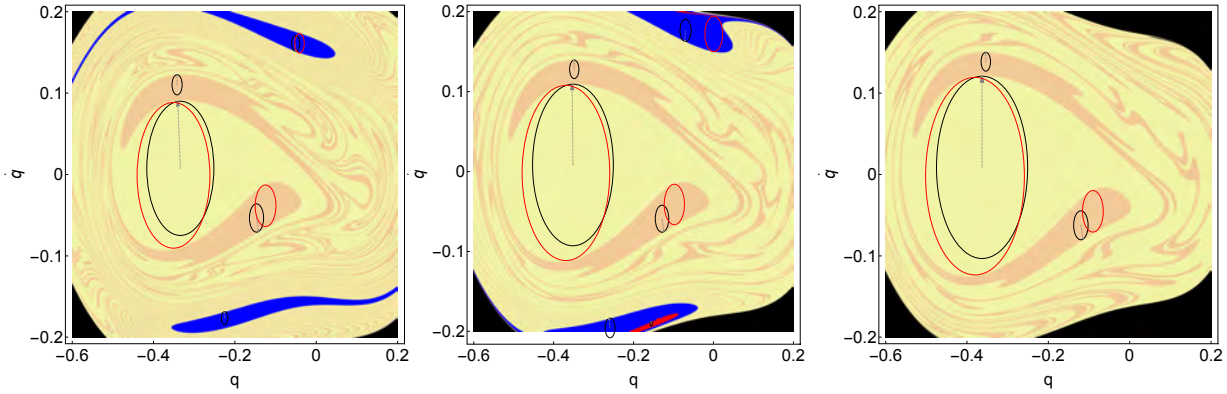

(a) $V_{DC} = 55.1895V$ (b) $V_{DC} = 55.3158V$ (c) $V_{DC} = 55.4V$

Figure 10: Basins of attraction for the secondary branch in presence of the bifurcated attractor. Integrity measures are reported within the picture. Black/red circles reports the LIM/IF measure. Fixed parameters $P = 3300Pa$, $V_{ac} = 0.1$, $\Omega/\omega_0 = 1$

The topology in proximity of the ultimate saddle-node point LP5 is illustrated with a sequence of basins of attraction in Figure 11. Approaching the ultimate snap-through point, the basin of the secondary branch progressively erodes (Figures $11(a,b)$). Figures $11(c,d)$ show the grow of the basin of the period-2 attractor (PD5/6) until the maximum extension at (Figure $11(e)$) where the

secondary basin is completely absent. The recovered basin at $V_{DC} = 56.89V$ shrinks towards null extension after $V_{DC} = 56.91V$.

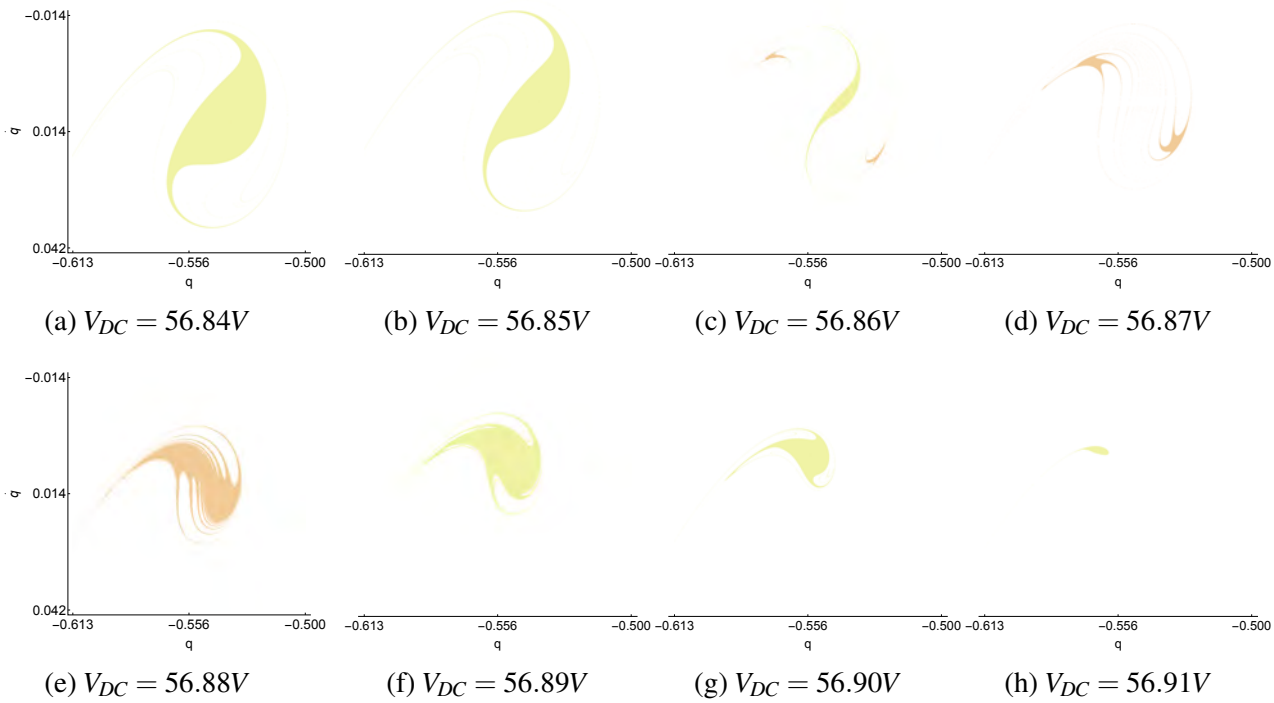

(a) $V_{DC} = 56.84V$ (b) $V_{DC} = 56.85V$ (c) $V_{DC} = 56.86V$ (d) $V_{DC} = 56.87V$

(e) $V_{DC} = 56.88V$ (f) $V_{DC} = 56.89V$ (g) $V_{DC} = 56.90V$ (h) $V_{DC} = 56.91V$

Figure 11: Basins of attraction in proximity of the ultimate saddle-node point LP5. Fixed parameters $P = 3300Pa$, $V_{ac} = 0.1$, $\Omega/\omega_0 = 1$

4. Conclusions

We investigated the global dynamics of an electrically-actuated micro pressure sensor. The combination of applied voltage and pressure depict bi-stable/multi-stable configurations, with the simultaneous presence of multiple instability events. The introduction of an alternating component in the electric actuation entails complex scenarios of bifurcation in which symmetry-breaking bifurcations undermines the stability of the micro-plate. By making use of basins of attraction the robustness of the motion close to instability has been unveiled. Integrity profiles show drastic unsafe windows in which small variation of the DC voltage greatly modifies the system response.

The present bifurcation analysis, performed by varying the DC voltage, is useful for the design of sensing devices. By exploiting sudden changes in the motion, coexisting attractors can be at the base of sensing mechanism and electrical actuators.

References

[1] W.-C. Chuang, H.-L. Lee, P.-Z. Chang, and Y.-C. Hu. Review on the modeling of electrostatic mems. *Sensors*, 10(6):6149–6171, 2010.

[2] C.-C. Nguyen. Vibrating rf mems for next generation wireless applications. In *Custom Integrated Circuits Conference, 2004. Proceedings of the IEEE 2004*, pages 257–264, 2004.

[3] J. F. Rhoads, S. W. Shaw, K. L. Turner, J. Moehlis, B. E. DeMartini, and W. Zhang. Generalized parametric resonance in electrostatically actuated microelectromechanical oscillators. *Journal of Sound and Vibration*, 296(4):797 – 829, 2006.

[4] D. Elata and S. Abu-Salih. Analysis of a novel method for measuring residual stress in micro-systems. *Journal of Micromechanics and Microengineering*, 15(5):921, 2005.

[5] B. Sajadi, F. Alijani, D. Davidovikj, J. Goosen, P. G. Steeneken, and F. van Keulen. Experimental characterization of graphene by electrostatic resonance frequency tuning. *Journal of Applied Physics*, 122(23):234302, 2017.

[6] D. Davidovikj, F. Alijani, S. J. Cartamil-Bueno, H. S. J. van der Zant, M. Amabili, and P. G. Steeneken. Nonlinear dynamic characterization of two-dimensional materials. *Nature Communications*, 8(1):1253, 2017.

[7] M. Younis. *MEMS Linear and Nonlinear Statics and Dynamics*. Microsystems. Springer US, 2011.

[8] V. Kumar, Y. Yang, J. W. Boley, G. T. C. Chiu, and J. F. Rhoads. Modeling, analysis, and experimental validation of a bifurcation-based microsensor. *Journal of Microelectromechanical Systems*, 21(3):549–558, June 2012.

[9] V. Kumar, J. W. Boley, Y. Yang, H. Ekowaluyo, J. K. Miller, G. T.-C. Chiu, and J. F. Rhoads. Bifurcation-based mass sensing using piezoelectrically-actuated microcantilevers. *Applied Physics Letters*, 98(15), 2011.

[10] V.-N. Nguyen, S. Baguet, C.-H. Lamarque, and R. Dufour. Bifurcation-based micro-/nanoelectromechanical mass detection. *Nonlinear Dynamics*, 79(1):647–662, 2015.

[11] P. Belardinelli, M. Ghatkesar, U. Staufer, and F. Alijani. Linear and non-linear vibrations of fluid-filled hollow microcantilevers interacting with small particles. *International Journal of Non-Linear Mechanics*, 93, 2017.

[12] U. Feudel. Complex Dynamics in Multistable Systems. *International Journal of Bifurcation and Chaos*, 18(06):1607–1626, 2008.

[13] A. M. Lyapunov. The general problem of the stability of motion. *International Journal of Control*, 55(3):531–534, 1992.

[14] G. Rega and S. Lenci. A global dynamics perspective for system safety from macro- to nanomechanics: Analysis, control, and design engineering. *Applied Mechanics Reviews*, 67(5):050802–050802, 10 2015.

[15] P. Belardinelli and S. Lenci. Improving the Global Analysis of Mechanical Systems via Parallel Computation of Basins of Attraction. In *Procedia IUTAM*, volume 22, 2017.

[16] P. Belardinelli and S. Lenci. An efficient parallel implementation of cell mapping methods for mdof systems. *Nonlinear Dynamics*, 86(4):1–12, 2016.

[17] P. Belardinelli and S. Lenci. A first parallel programming approach in basins of attraction computation. *International Journal of Non-Linear Mechanics*, 80:76–81, 2016.

[18] W.-M. Zhang, H. Yan, Z.-K. Peng, and G. Meng. Electrostatic pull-in instability in mems/nems: A review. *Sensors and Actuators A: Physical*, 214:187–218, 2014.

[19] S. Chowdhury, M. A. Ahmadi, and W. C. Miller. Pull-in voltage calculations for mems sensors with cantilevered beams. In *IEEE-NEWCAS Conference, 2005. The 3rd International*, pages 143–146. IEEE, 2005.

[20] B. Sajadi, F. Alijani, H. Goosen, and F. van Keulen. Effect of pressure on nonlinear dynamics and instability of electrically actuated circular micro-plates. *Nonlinear Dynamics*, Dec 2017.

[21] A. H. Nayfeh, M. I. Younis, and E. M. Abdel-Rahman. Dynamic pull-in phenomenon in mems resonators. *Nonlinear dynamics*, 48(1-2):153–163, 2007.

[22] L.-D. Liao, P. C. Chao, C.-W. Huang, and C.-W. Chiu. Dc dynamic and static pull-in predictions and analysis for electrostatically actuated clamped circular micro-plates based on a continuous model. *Journal of Micromechanics and Microengineering*, 20(2):025013, 2010.

[23] G. W. Vogl and A. H. Nayfeh. A reduced-order model for electrically actuated clamped circular plates. *Journal of Micromechanics and Microengineering*, 15(4):684, 2005.

[24] J. Lardies, M. Berthillier, and M. L. Bellaredj. Analytical investigation of the pull-in voltage in capacitive mechanical sensors. In *SPIE Microtechnologies*, pages 80661N–80661N–10. International Society for Optics and Photonics, 2011.

[25] P. Belardinelli, S. Lenci, and L. Demeio. A comparison of different semi-analytical techniques to determine the nonlinear oscillations of a slender microbeam. *Meccanica*, 49(8), 2014.

[26] P. Belardinelli, S. Lenci, and M. Brocchini. Modeling and analysis of an electrically actuated microbeam based on nonclassical beam theory. *Journal of Computational and Nonlinear Dynamics*, 9(3), 2014.

[27] B. Sajadi, F. Alijani, H. Goosen, and F. van Keulen. Static and dynamic pull-in of electrically actuated circular micro-membranes. In *ASME 2016 International Mechanical Engineering Congress and Exposition*, pages V04AT05A030–V04AT05A030. American Society of Mechanical Engineers.

[28] B. Sajadi, J. Goosen, and F. van Keulen. Bi-stability of micro-plates: A sensitive mechanism for differential pressure measurements. *Applied Physics Letters*, 111(12):124101–1–5, 2017.

[29] Z. Li, L. Zhao, Z. Ye, H. Wang, Y. Zhao, and Z. Jiang. Resonant frequency analysis on an electrostatically actuated microplate under uniform hydrostatic pressure. *Journal of Physics D: Applied Physics*, 46(19):195108, 2013.

[30] A. H. Nayfeh, M. I. Younis, and E. M. Abdel-Rahman. Reduced-order models for mems applications. *Nonlinear dynamics*, 41(1-3):211–236, 2005.

[31] D. I. Caruntu and R. Oyervides. Frequency response reduced order model of primary resonance of electrostatically actuated mems circular plate resonators. *Communications in Nonlinear Science and Numerical Simulation*, 43:261–270, 2017.

[32] E. J. Doedel, A. R. Champneys, T. F. Fairgrieve, Y. A. Kuznetsov, B. Sandstede, and X. Wang. Auto97, 1998.

[33] S. Lenci and G. Rega. Competing Dynamic Solutions in a Parametrically Excited Pendulum: Attractor Robustness and Basin Integrity. *Journal of Computational and Nonlinear Dynamics*, 3(4):041010, 2008.

[34] D. I. Caruntu and R. Oyervides. Voltage response of primary resonance of electrostatically actuated mems clamped circular plate resonators. *Journal of Computational and Nonlinear Dynamics*, 11(4):041021, 2016.

[35] M. Amabili. *Nonlinear vibrations and stability of shells and plates*. Cambridge University Press, 2008.

[36] F. Alijani and M. Amabili. Non-linear static bending and forced vibrations of rectangular plates retaining non-linearities in rotations and thickness deformation. *International Journal of Non-Linear Mechanics*, 67:394–404, 2014.

[37] L. W. Refwield. Nonlinear flexural oscillations of shallow arches. *AIAA Journal*, 12(1):91–93, 2017/12/07 1974.

[38] M. Zakrževskis. New concepts of nonlinear dynamics: Complete bifurcation groups, protuberances, unstable periodic infinitiums and rare attractors. *Journal of Vibroengineering*, 10:421–441, 2008.

[39] P. Belardinelli, S. Lenci, and G. Rega. Seamless variation of isometric and anisometric dynamical integrity measures in basins's erosion. *Communications in Nonlinear Science and Numerical Simulation*, 56(Supplement C):499 – 507, 2018.